Predictions for $\sqrt{s_{NN}} = 5.02$ TeV Pb + Pb collisions from a multiphase transport model

Guo-Liang Ma*
Shanghai Institute of Applied Physics, Chinese Academy of Sciences, Shanghai 201800, China

Zi-Wei Lin†
Department of Physics, East Carolina University, Greenville, North Carolina 27858, USA
(Received 4 February 2016; revised manuscript received 1 April 2016; published 23 May 2016)

We present predictions from the string melting version of a multiphase transport model on various observables in Pb+Pb collisions at $\sqrt{s_{NN}} = 5.02$ TeV. We use the same version of the model as an earlier study that reasonably reproduced dN/dy, p_T spectra and elliptic flow of charged pions and kaons at low-p_T for central and semicentral heavy ion collisions at 200 GeV and 2.76 TeV. While we compare with the already-available centrality dependence data on charged particle $dN/d\eta$ at mid-pseudorapidity in Pb+Pb collisions at 5.02 TeV, we make predictions on identified particle dN/dy, p_T spectra, azimuthal anisotropies $v_n(n = 2,3,4)$, and factorization ratios $r_n(\eta^a,\eta^b)(n = 2,3)$ for longitudinal correlations.

DOI: 10.1103/PhysRevC.93.054911

I. INTRODUCTION

Ultrarelativistic heavy ion collisions at the BNL Relativistic Heavy Ion Collider (RHIC) and the CERN Large Hadron Collider (LHC) have created a dense matter consisting of partonic degrees of freedom, often called the quark-gluon plasma (QGP). From comparisons between the experimental data on various observables and results of different theoretical models, we expect to learn the space-time evolution of the dense matter and consequently the properties of QGP and quantum chromodynamics. For collisions of heavy ions such as Pb+Pb, the highest energy achievable in the near future is $\sqrt{s_{NN}} = 5.02$ TeV. Since high energy heavy ion collisions are expected to create a QGP matter with a high initial effective temperature with a long lifetime being in parton degrees of freedom, comparing observables at this highest energy with those at lower energies will provide us new information for the study of QGP properties.

Simulations of the space-time evolution of relativistic heavy ion collisions have been performed extensively with hydrodynamic models [1–3], transport models [4–6], and hybrid models that combine a hydrodynamic model with a transport model [7–9]. Despite the different physics foundations and assumptions in these three types of models, they have been quite successful in describing many observables such as azimuthal anisotropies. It has been widely believed that for heavy colliding systems transport models essentially approach the hydrodynamical limit, therefore it does not seem surprising that transport and hydrodynamic models can both describe anisotropy observables in large systems. On the other hand, it is puzzling that they also both seem to describe azimuthal anisotropies in small systems such as $p + \mathrm{Pb}$ and $d + \mathrm{Au}$ collisions [10–12], since transport models are far from the hydrodynamical limit for small systems.

Recently it was realized that transport models for current ultrarelativistic heavy colliding systems may still be far from the hydrodynamical limit. In particular, it is found with transport models [13,14] that azimuthal anisotropies may be produced mainly by the anisotropic parton escape probability as a response to the initial spatial eccentricity through interactions, not mainly by the hydrodynamic-type collective flow. Therefore transport models and hydrodynamic models for current heavy ion collisions are different, and it is important to identify unique signatures of transport or hydrodynamic models in order to determine which picture is a more relevant description for a given type of heavy ion collisions. There have been recent hydrodynamic predictions for 5.02 TeV Pb+Pb collisions [15,16], and in this study we present transport predictions from a multiphase transport (AMPT) model [5].

II. THE STRING MELTING VERSION OF THE AMPT MODEL AND ITS PARAMETERS

The AMPT model was constructed to simulate relativistic heavy ion collisions, and predictions were made for Au+Au collisions at RHIC energies [17–19]. The model at that time (now called the default version) consisted of fluctuating initial conditions from the HIJING model [20], the elastic parton cascade ZPC [21] for minijet partons, the Lund string model [22] for hadronization, and the ART hadron cascade [23]. With modified Lund string fragmentation a and b parameters [5,19], the default AMPT model was able to reasonably describe the rapidity distributions and p_T spectra in heavy ion collisions from CERN Super Proton Synchrotron (SPS) to RHIC energies.

It was later found that the default version of the AMPT model (as all transport models at the time) underestimated the elliptic flow observed at RHIC, and the reason was that most of the energy produced in the overlap volume of heavy ion collisions are in hadronic strings and thus not included in the parton cascade in the model [24]. So the string melting version of the AMPT model was constructed, where all excited hadronic strings in the overlap volume are converted into partons [24]. The string melting AMPT model consists of

*glma@sinap.ac.cn
†linz@ecu.edu

fluctuating initial conditions from the HIJING model [20], the elastic parton cascade ZPC [21] for all partons from the melting of hadronic strings, a quark coalescence model for hadronization, and the ART hadron cascade [23]. Due to its dense parton phase, the string melting version reasonably fit the elliptic flow [24] and two-pion interferometry [25] in heavy ion collisions at RHIC energies; but it could not reproduce well the rapidity distributions and p_T spectra (when using the same Lund a and b parameters as in the default version). Therefore, in previous predictions from the AMPT model on Pb+Pb collisions at 5.5 TeV [26], we used the default AMPT model to predict particle yields and p_T spectra but used the string melting AMPT model to predict the elliptic flow and two-pion or two-kaon correlation functions.

Recently we found that the string melting AMPT model can be tuned to reasonably reproduce the pion and kaon yields, p_T spectra, and elliptic flows below $\sim$1.5 GeV/c in central and semicentral Au+Au collisions at the RHIC energy of $\sqrt{s_{NN}} = 200$ GeV and Pb+Pb collisions at the LHC energy of 2.76 TeV [27]. For predictions for the top LHC energy of 5.02 TeV in this study, we use the same string melting AMPT version (v2.26t5, available online [28]) and the same parameter values as used for the LHC energy of 2.76 TeV in an earlier study [27]. These parameters include the Lund string fragmentation parameters $a = 0.30$ and $b = 0.15$ GeV^{-2}, strong coupling constant $\alpha_s = 0.33$, and a parton cross section of 3 mb. Note that this AMPT version [27,28] imposes an upper limit of 0.40 on the relative production of strange to nonstrange quarks from the Lund string fragmentation. In addition, in order to avoid potential effects due to different Lund a values, we also use these parameters (Lund $a = 0.30$ in particular) for the 200 GeV RHIC simulations in this study, even though they describe the 200 GeV dN/dy data not as well as the earlier study [27] which used Lund $a = 0.55$. Since our predictions include observables far away from mid-(pseudo)rapidity, we terminate the hadron cascade at 200 fm/c in all AMPT calculations of this study instead of the typical value of 30 fm/c. Note that centrality in AMPT results of this study is determined by the range of impact parameters in the simulated minimum-bias events for which we impose no upper limit on the maximum impact parameter. For example, for Pb+Pb collisions at 5.02 TeV the 0–5% centrality corresponds to impact parameters from 0 to 3.6 fm while the 20–30% centrality corresponds to impact parameters from 7.3 fm to 8.9 fm.

III. COMPARISON OF AMPT RESULTS WITH THE AVAILABLE $dN_{ch}/d\eta$ DATA

We compare in Fig. 1 charged particle yields at mid-pseudorapidity, scaled by half the number of participant nucleons $N_{\rm part}$, from the string melting AMPT model (curves without symbols) in comparison with the experimental data, which include the ALICE Pb+Pb data at $\sqrt{s_{NN}} = 5.02$ TeV [29], 2.76 TeV [30], and the PHENIX Au+Au data at 200 GeV [31]. Although these AMPT results were already obtained with the same AMPT code and parameters as in an earlier study [27] before the announcement of the ALICE 5.02 TeV data [29], they were not posted before the data and are thus, strictly speaking, not predictions.

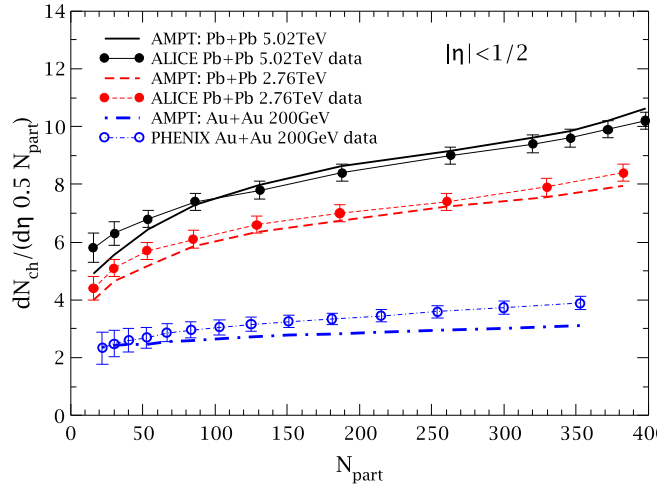

FIG. 1. The centrality dependence of $dN_{ch}/d\eta$ at mid-pseudorapidity ($|\eta| < 1/2$) from the string melting AMPT model in comparison with data for heavy ion collisions at $\sqrt{s_{NN}} = 5.02$ TeV, 2.76 TeV, and 200 GeV.

Figure 1 shows that the AMPT model reproduces the overall magnitudes and the $N_{\rm part}$ dependence shapes of $dN_{ch}/d\eta$ at mid-pseudorapidity ($|\eta| < 1/2$). Note that the AMPT 200 GeV results in this study are obtained using the same Lund a parameter ($a = 0.30$) as the LHC results; they are generally lower than the PHENIX data and also lower than the AMPT 200 GeV results in an earlier study [27] where the Lund parameter $a = 0.55$ was used. We also see in Fig. 1 that the energy dependence of $dN_{ch}/d\eta$ at mid-pseudorapidity from AMPT is often stronger than the data. This can be better demonstrated in Fig. 2, where we show the ratio of mid-pseudorapidity $dN_{ch}/d\eta$ at one energy to that at a lower energy. The ratio of mid-pseudorapidity $dN_{ch}/d\eta$ in Pb+Pb collisions at 2.76 TeV to that in Au+Au collisions at

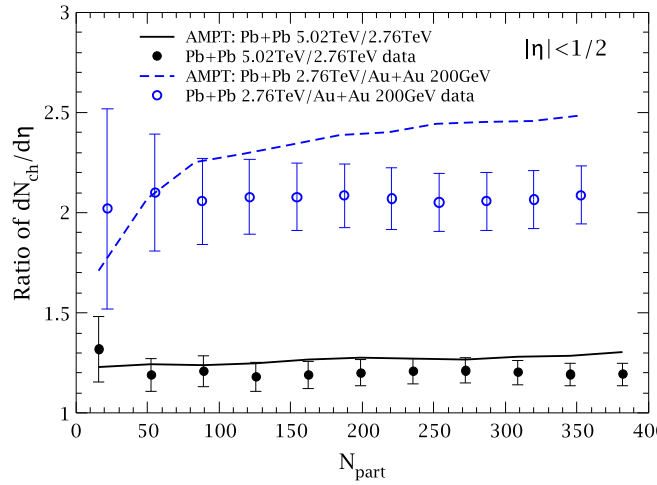

FIG. 2. Ratio of mid-pseudorapidity $dN_{ch}/d\eta$ at two different energies from AMPT in comparison with the corresponding ratio derived from experimental data.

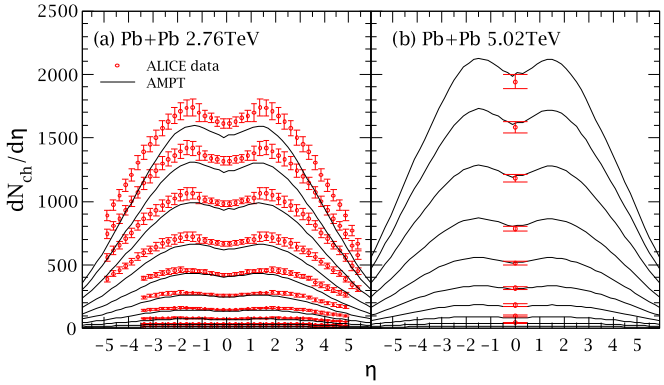

FIG. 3. $dN_{ch}/d\eta$ from the string melting AMPT model for Pb+Pb collisions at (a) $\sqrt{s_{NN}} = 2.76$ TeV and (b) 5.02 TeV in comparison with data (circles). Curves from top to bottom represent, respectively, the AMPT results for the following centralities: 0–5%, 5–10%, 10–20%, 20–30%, 30–40%, 40–50%, 50–60%, 60–70%, 70–80%, and 80–90%.

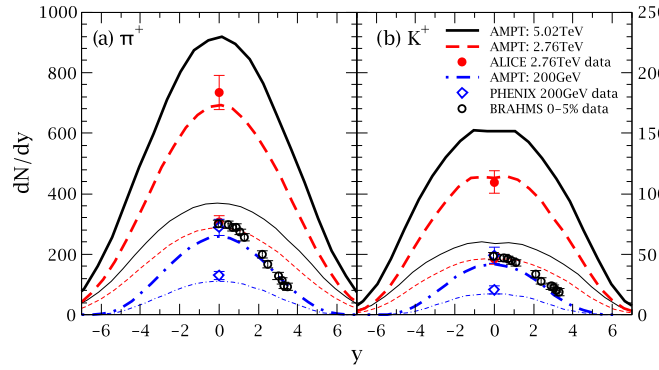

FIG. 4. AMPT results on dN/dy of (a) π^+ and (b) K^+ for Pb+Pb collisions at 5.02 TeV, 2.76 TeV and Au+Au collisions at 200 GeV, in comparison with experimental data at 2.76 TeV and 200 GeV, for 0–5% and 20–30% centralities.

200 GeV from AMPT (dashed curve) is usually higher than the corresponding data (open circles), where the data represent the ratio of the ALICE data for Pb+Pb collisions at 2.76 TeV to the PHENIX data for Au+Au collisions at 200 GeV. On the other hand, the ratio of mid-pseudorapidity $dN_{ch}/d\eta$ in Pb+Pb collisions at 5.02 TeV to that at 2.76 TeV from AMPT (solid curve) is close to the corresponding data, and its magnitude is much lower than the other ratio (dashed curve) as a result of the smaller relative increase of the collision energy. Note that, since the experimental data (and AMPT results) in Fig. 1 at different energies have different sets of $N_{\rm part}$ values, we have used linear interpolation in order to make the $dN_{ch}/d\eta$ ratio at a given $N_{\rm part}$ value for Fig. 2.

The $dN_{ch}/d\eta$ results as functions of η at different centralities of Pb+Pb collisions are shown in Fig. 3(a) for $\sqrt{s_{NN}} =$ 2.76 TeV and in Fig. 3(b) for 5.02 TeV. Solid curves from top to bottom in each panel represent, respectively, the AMPT results for the following centralities: 0–5%, 5–10%, 10–20%, 20–30%, 30–40%, 40–50%, 50–60%, 60–70%, 70–80%, and 80–90%; while circles represent the corresponding ALICE data [29,32,33]. Note that the ALICE data at 5.02 TeV [29] represent the $dN_{ch}/d\eta$ values at mid-pseudorapidity ($|\eta| < 1/2$) and they do not include the 80–90% centrality. We see that the AMPT model reproduces the overall $dN_{ch}/d\eta$ shape, but the AMPT $dN_{ch}/d\eta$ curves at 2.76 TeV are a bit narrower than the corresponding data.

IV. AMPT PREDICTIONS

This section shows our predictions on dN/dy and p_T spectra of identified particles including π^+ and K^+, azimuthal anisotropies including the p_T dependences of $v_n(n = 2,3,4)$ and η dependences of v_2, and the factorization ratios $r_2(\eta^a,\eta^b)$ and $r_3(\eta^a,\eta^b)$ for longitudinal correlations.

A. Identified particle dN/dy

AMPT results of π^+ and K^+ dN/dy are shown in Figs. 4(a) and 4(b), respectively, where thick curves represent the 0–5% centrality and thin curves represent the 20–30% centrality. Experimental data for Pb+Pb collisions at 2.76 TeV (filled symbols) and Au+Au collisions at 200 GeV (open symbols) are also shown for comparison with the corresponding AMPT results (dashed curves for 2.76 TeV and dot-dashed curves for 200 GeV). We see reasonable agreements between the AMPT results and the midrapidity ALICE data at 2.76 TeV [34] and PHENIX data at 200 GeV [35] for both centralities. Reasonable agreements are also seen in comparison with the BRAHMS rapidity dependence data for 0–5% central Au+Au collisions at 200 GeV [36]. Note that the pion and kaon yields from PHENIX and ALICE have been corrected for weak decays (especially those of strange baryons) and can thus be directly compared with AMPT results.

When the energy of Pb+Pb collisions increases from 2.76 TeV to 5.02 TeV, we see from Fig. 4 that the π^+ dN/dy at midrapidity increases by ~33% for the 0–5% centralilty and ~28% for the 20–30% centrality, while the increase for K^+ is ~34% for the 0–5% centrality and ~28% for the 20–30% centrality.

B. Identified particle p_T spectra

AMPT results on the π^+ and K^+ p_T spectra are shown in Fig. 5 for 0–5% central Pb+Pb collisions at 5.02 TeV (solid curves), 2.76 TeV (dashed curves), and 0–5% Au+Au collisions at 200 GeV (dot-dashed curves). The 0–5% ALICE data at 2.76 TeV [34] and 0–5% PHENIX data at 200 GeV [35] are shown by symbols. We see that the AMPT model roughly reproduces the observed p_T spectra at low p_T at the lower two energies.

To better observe the change of the p_T spectra, we show in Fig. 6 the ratio of the midrapidity p_T spectrum at one energy to that at a lower energy. The AMPT ratio of Pb+Pb collisions at 5.02 TeV to those at 2.76 TeV (solid curves) shows a weak increase with p_T (from ~1.3 at $p_T = 0$ to ~1.4 at $p_T = 2$ GeV/c) for both π^+ and K^+, indicating that the p_T spectrum becomes slightly harder with the increase in energy. In comparison, the hardening of the p_T spectra as well as the overall increase in magnitude are much stronger going from central Au+Au collisions at 200 GeV to central Pb+Pb

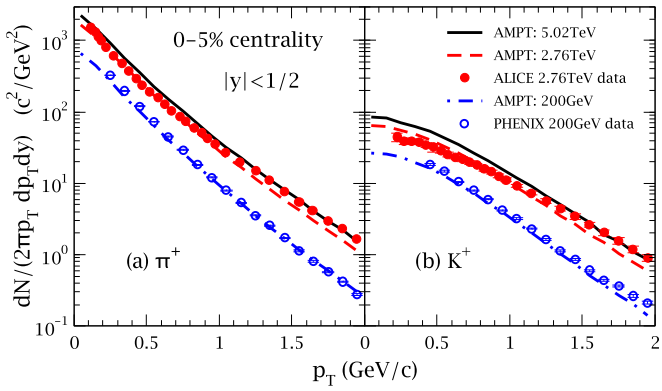

FIG. 5. AMPT results on (a) π^+ and (b) K^+ p_T spectra at midrapidity in Pb+Pb collisions at 5.02 TeV, 2.76 TeV, and Au+Au collisions at 200 GeV, in comparison with available experimental data, for the 0–5% centrality.

collisions at 2.76 TeV. However, the AMPT results (dashed curves) underestimate the hardening of the p_T spectra when compared with the experimental data (circles).

C. Azimuthal anisotropies

Azimuthal anisotropies such as v_2, v_3, and v_4 reflect the response to the initial spatial eccentricities, which are generated by the overall geometry in noncentral collisions and/or fluctuations, through interactions during the evolution of the dense matter. Detailed studies of these anisotropic flow observables enable us to study whether the system is close to hydrodynamics [13,14] and to extract the QGP properties [1–3] if the system is close to the hydrodynamic limit.

In this study we use two methods to calculate the azimuthal anisotropies. For Au+Au collisions at 200 GeV, we use the event-plane method to calculate $v_n\{\mathrm{EP}\}$, in order to compare with the PHENIX data. We calculate the nth event plane Ψ_n based on the momentum information of final particles [37]:

$$\Psi_n = \frac{1}{n}\left(\arctan\frac{\langle p_T \sin(n\phi)\rangle}{\langle p_T \cos(n\phi)\rangle}\right), \tag{1}$$

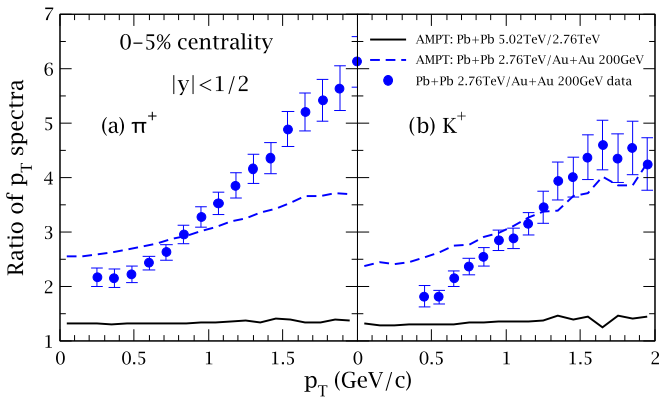

FIG. 6. Ratio of p_T spectra at midrapidity at two different energies from AMPT in comparison with data for the 0–5% centrality for (a) π^+ and (b) K^+.

where ϕ represents the azimuthal angle of a particle's momentum, and $\langle\cdots\rangle$ denotes the average over particles used for the event plane calculation. Then the nth anisotropy coefficient, $v_n\{\mathrm{EP}\}$, can be obtained as

$$v_n\{\mathrm{EP}\} = \langle\cos[n(\phi - \Psi_n)]\rangle/\mathrm{Res}\{\Psi_n\}, \tag{2}$$

where $\mathrm{Res}\{\Psi_n\}$ is the nth event plane resolution calculated by the experimental subevent method. We use all particles within the acceptance of PHENIX event plane detectors, $1.0 < |\eta| < 2.8$, to reconstruct the event plane. For Pb+Pb collisions at 2.76 and 5.02 TeV, we use the two-particle method with a large $\Delta\eta$ gap to calculate $v_n\{2\}$, similar to the CMS [38] and the ATLAS [39] methods [except for $v_2(\eta)$ calculations as shown in Figs. 11 and 12 where we use the event-plane method]. The two-particle azimuthal $\Delta\phi$ correlation function is decomposed as

$$\frac{1}{N_{\mathrm{trig}}}\frac{dN^{\mathrm{pair}}}{d\Delta\phi} = \frac{N_{\mathrm{assoc}}}{2\pi}\left[1 + \sum_n 2V_{n\Delta}\cos(n\Delta\phi)\right], \tag{3}$$

where $V_{n\Delta}$ is the Fourier coefficient and N_{assoc} represents the total number of pairs per trigger particle. A cut of $|\Delta\eta| > 2$ is applied to remove short-range correlations from jet fragmentation for charged particles within $|\eta| < 2.5$. The azimuthal anisotropy coefficients, $v_n\{2, |\Delta\eta| > 2\}$, from the two-particle correlation method can be extracted as a function of p_T from the fitted Fourier coefficients as

$$v_n\{2, |\Delta\eta| > 2\}(p_T) = \frac{V_{n\Delta}(p_T, p_T^{\mathrm{ref}})}{\sqrt{V_{n\Delta}(p_T^{\mathrm{ref}}, p_T^{\mathrm{ref}})}}, \tag{4}$$

where a fixed p_T^{ref} range for the "reference particles" is chosen to be $0.3 < p_T < 3.0$ GeV/c in our study. It have been found that the two methods give very similar results [39,40].

AMPT results on the p_T dependence of v_2 at midrapidity are shown in Fig. 7(a) for charged pions and Fig. 7(b) for charged kaons, in comparison with the ALICE data for Pb+Pb collisions at 2.76 TeV (filled circles) and PHENIX data for Au+Au collisions at 200 GeV (open circles) [40], for the 20–30% centrality. The 200 GeV AMPT results has the cut $|\eta| < 0.35$ for comparison with the PHENIX data. We see that

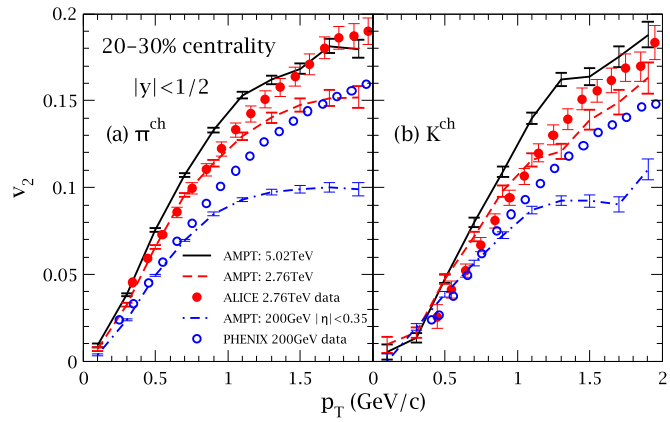

FIG. 7. The p_T dependence of v_2 at midrapidity from AMPT, in comparison with available experimental data, for the 20–30% centrality for (a) charged pions and (b) charged kaons.

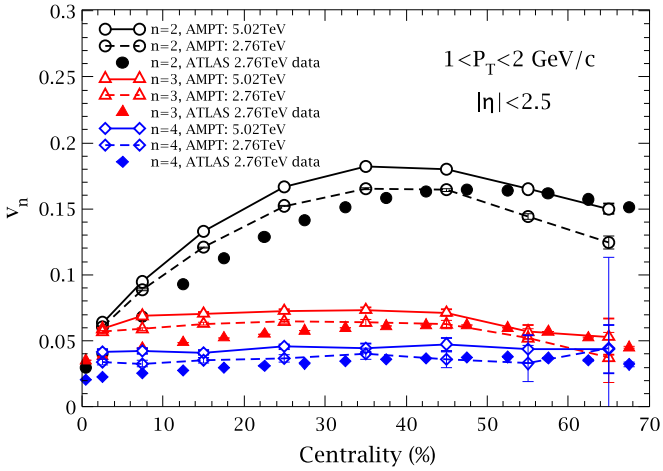

FIG. 8. Centrality dependences of charged particle $v_n(n = 2,3,4)$ within $1 < p_T < 2$ GeV/c and $|\eta| < 2.5$ from AMPT for Pb+Pb collisions in comparison with the ATLAS data at 2.76 TeV.

the AMPT model reasonably reproduces the v_2 data below $p_T \sim 1$ GeV/c at these two energies. For Pb+Pb collisions at 5.02 TeV in comparison with those at 2.76 TeV, the AMPT model predicts that the pion v_2 has a relative increase of ~16% that is rather insensitive to p_T within 0 and 2 GeV/c, while the relative increase of the kaon v_2 shows an overall increase with p_T within this p_T range.

Figure 8 shows the centrality dependences of charged particle v_2, v_3, and v_4 within $1 < p_T < 2$ GeV/c and $|\eta| < 2.5$ for Pb+Pb collisions at LHC energies. From the comparison between the AMPT results at 2.76 TeV (dashed curves with open symbols) and the corresponding ATLAS data [39] (filled symbols), the AMPT model is seen to reasonably reproduce the overall shapes and magnitudes of v_2, v_3, and v_4. We also see that, for each n, the AMPT v_n magnitude at 5.02 TeV is almost always higher than that at 2.76 TeV at the same centrality. In Fig. 9 we show the ratio of the AMPT $v_n(n = 2,3,4)$ result at 5.02 TeV to that at 2.76 TeV, where points with very large

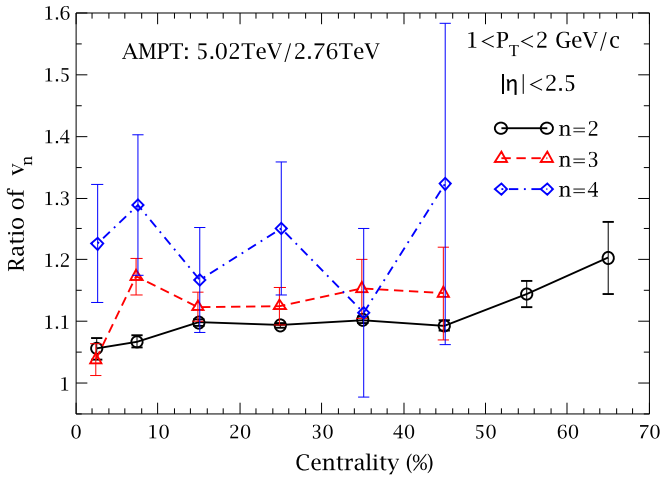

FIG. 9. Ratio of the centrality dependence of charged particle $v_n(n = 2,3,4)$ within $1 < p_T < 2$ GeV/c and $|\eta| < 2.5$ at two different energies from AMPT.

error bars have been removed and the curves for $n = 3$ and $n = 4$ are slightly shifted horizontally (by ±0.1%) for easier identification. We see that the overall relative increase is the smallest for v_2 but the largest for v_4; this ordering of the relative v_n increase is the same as that in the two recent hydrodynamic predictions [15,16]. In addition, an overall centrality dependence of the relative increase is observed for v_2 from the AMPT results, where more peripheral collisions tend to have a larger relative increase; this is also consistent with the two recent hydrodynamic predictions. The magnitudes of the relative increases in v_2 from AMPT as shown in Fig. 9 are bigger than those in the two hydrodynamic predictions [15,16], since different p_T ranges are used in those calculations.

AMPT results on the p_T dependences of charged particle v_2, v_3, and v_4 within $|\eta| < 2.5$ are shown in Fig. 10 for Pb+Pb collisions at 5.02 TeV (solid curves with open symbols) and 2.76 TeV (dashed curves with open symbols) over a large p_T range for eight different centralities. The ATLAS data for Pb+Pb collisions at 2.76 TeV [39] (thin dashed curves with filled symbols) are also shown for comparison. Overall, the AMPT model reasonably reproduces the shapes and magnitudes of v_n at 2.76 TeV (especially below $p_T \sim 3$ GeV/c), including the ordering of v_n at a given centrality. For v_2 below $p_T \sim 2$ GeV/c, we see that the AMPT model tends to overestimate for central collisions but underestimate for peripheral collisions, consistent with the centrality dependences of charged particle v_2 shown in Fig. 8. On the other hand, AMPT results on the p_T dependences of charged particle v_3 and v_4 at low p_T are quite consistent with the data at 2.76 TeV (except for central collisions).

We have also studied the pseudorapidity dependence of charged particle v_2. For the η dependence, we calculate v_2 using the event-plane method similar to the experiments. We use the η range $2.05 < |\eta| < 3.2$ for Au+Au collisions at 200 GeV as the PHOBOS experiment and $3 < |\eta| < 5$ for Pb+Pb collisions at 2.76 TeV as the CMS experiment for the event plane calculations. Note that the ATLAS range $3.2 < |\eta| < 4.8$ is similar to the above CMS range, and for LHC energies we use the event plane from the η side opposite to the charged particles used for the v_2 calculation. Figure 11 shows the AMPT results for Pb+Pb collisions at 5.02 TeV (solid curves), 2.76 TeV (dashed curves), and Au+Au collisions at 200 GeV (dot-dashed curves) for two centralities: 15–25% and 25–50%. The corresponding experimental data from CMS [41] (filled circles) and ATLAS [42] (open circles) for Pb+Pb collisions at 2.76 TeV and from PHOBOS [43] (open diamonds) for Au+Au collisions at 200 GeV are shown for comparison. We see that the AMPT model reasonably reproduces the observed magnitudes and shapes for these collisions at both centralities.

Figure 12 shows the ratios of charged particle $v_2(\eta)$ at one energy to that at a lower energy in the overlapping η range, including the range $5 < |\eta| < 6$. We see that in general the ratio is the lowest at $\eta = 0$ and gradually increases away from mid-pseudorapidity (at least up to $|\eta| \sim 2$), and the ratio curves are essentially the same for the two centrality classes. For the ratio of $v_2(\eta)$ in Pb+Pb collisions at 2.76 TeV to that in Au+Au collisions at 200 GeV, the AMPT results (thick dashed curve for the 15–25% centrality and thin dashed curve for the 25–50% centrality) are close to the data, considering

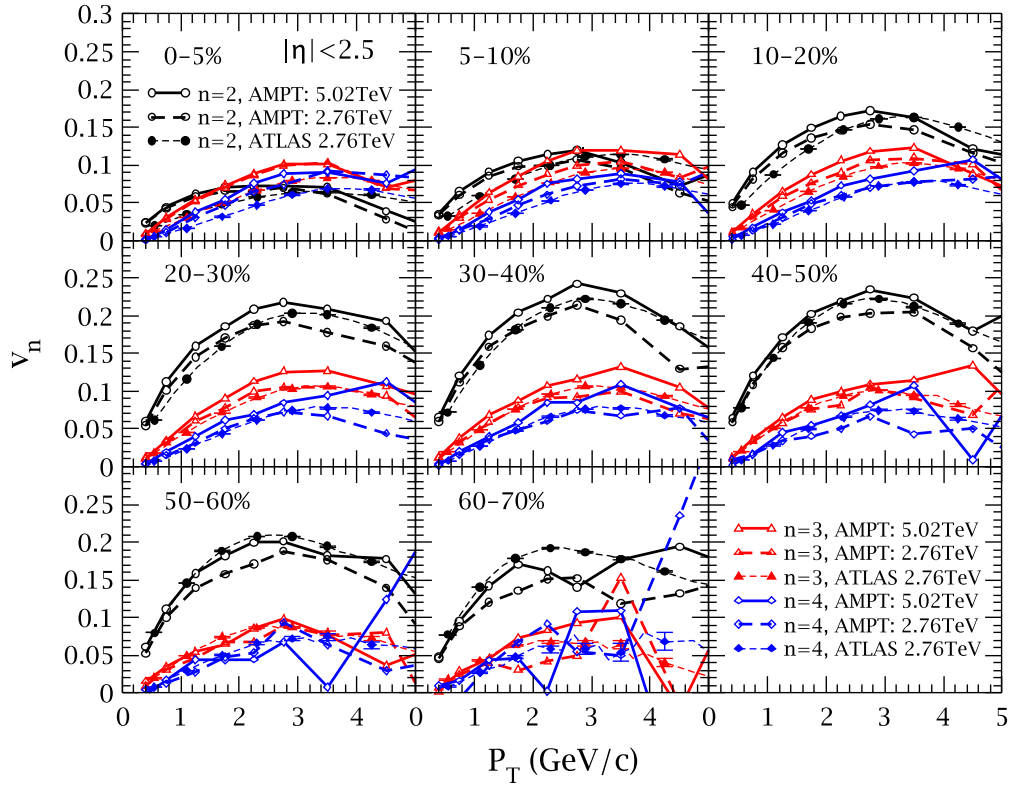

FIG. 10. The p_T dependences of charged particle $v_n(n = 2,3,4)$ within $|\eta| < 2.5$ at different centralities from AMPT for Pb+Pb collisions in comparison with the ATLAS data at 2.76 TeV.

the large error bars of the data. For the ratio of $v_2(\eta)$ in Pb+Pb collisions at 5.02 TeV to that at 2.76 TeV (solid curves), the AMPT results show that the overall magnitudes are lower than the other ratio (dashed curves).

D. Longitudinal correlations

The initial spatial geometry including the event plane depends on the pseudorapidity but also has longitudinal correlations [44–46]. This longitudinal correlation comes naturally in the AMPT model since each wounded nucleon can produce multiple initial particles that have almost the same transverse position but a range of different η values. For the string melting version of AMPT, each wounded nucleon typically produces many initial partons, therefore the initial transverse spatial geometry of the parton matter including the event plane has a strong correlation over a finite η range. Through partonic and hadronic interactions, the azimuthal anisotropies v_n will then have correlations over a finite η range.

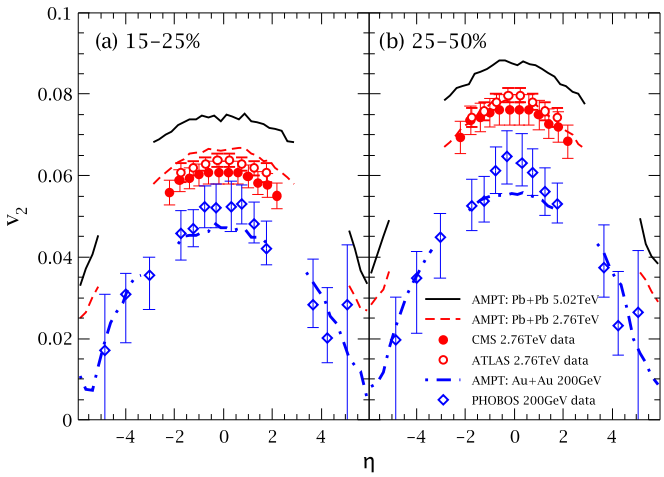

FIG. 11. AMPT results on the η dependence of v_2, in comparison with available experimental data, for (a) the 15–25% centrality and (b) the 25–50% centrality.

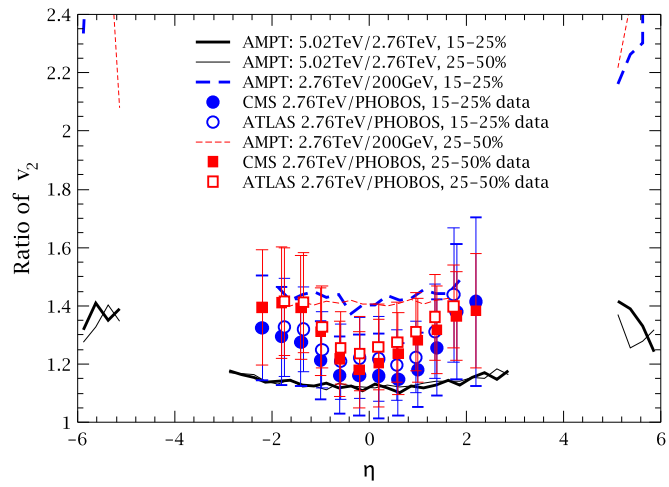

FIG. 12. Ratio of $v_2(\eta)$ at two different energies from AMPT in comparison with available experimental data.

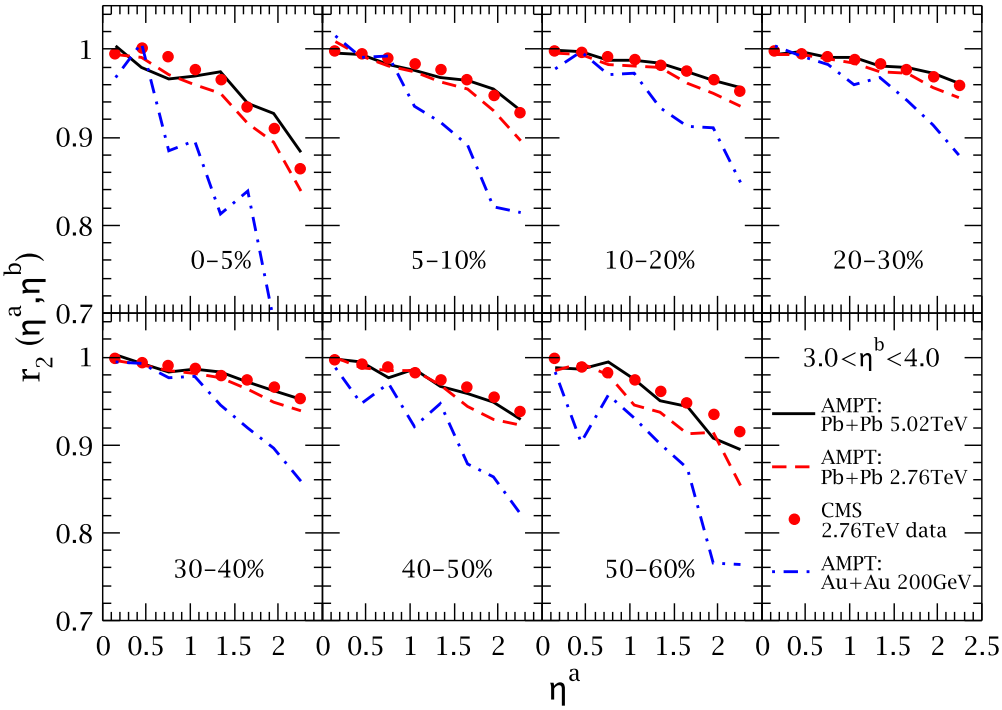

FIG. 13. AMPT results on the factorization ratio $r_2(\eta^a,\eta^b)$ as functions of η^a in comparison with the CMS 2.76 TeV data for different centralities.

We follow the definition of the correlation observable as proposed by the CMS collaboration [47]. The pseudorapidity range of reference particles is $3.0 < \eta^b < 4.0$ here. The factorization ratio $r_n(\eta^a,\eta^b)$ is calculated as

$$r_n(\eta^a,\eta^b) \equiv \frac{V_{n\Delta}(-\eta^a,\eta^b)}{V_{n\Delta}(\eta^a,\eta^b)}, \tag{5}$$

where $V_{n\Delta}(\eta^a,\eta^b)$ is defined as $\langle\langle\cos(n\Delta\phi)\rangle\rangle_S - \langle\langle\cos(n\Delta\phi)\rangle\rangle_B$. Here, $\langle\langle\rangle\rangle$ denotes the averaging over all particle pairs in each event and over all the events. The subscript S corresponds to the average over pairs taken from the same event, while B represents the mixing of particles from two randomly selected events from the same centrality class.

AMPT results on the factorization ratio $r_2(\eta^a,\eta^b)$ as a function of η^a are shown in Fig. 13 for Pb+Pb collisions at 5.02 TeV (solid curves), 2.76 TeV (dashed curves), and Au+Au collisions at 200 GeV (dot-dashed curves) for seven different centralities. We see that the AMPT results at 2.76 TeV are rather consistent with the corresponding CMS data [47], similar to an earlier study [46] that used the string melting AMPT model as the initial condition for an ideal (3 + 1)D hydrodynamics. Furthermore, the AMPT results show that the longitudinal correlation is much suppressed in pseudorapidity for Au+Au collisions at 200 GeV, again similar to the earlier study [46].

Comparing AMPT results at 5.02 TeV with those at 2.76 TeV, we see that the longitudinal correlation at 5.02 TeV is slightly stronger. This can be better seen in Fig. 14, which shows the ratios of $r_2(\eta^a,\eta^b)$ at 5.02 TeV to that at 2.76 TeV for most centrality classes. In addition, Fig. 14 shows that the increase of the ratio with η^a systematically depends on the centrality, with central collisions having the strongest relative increase of $r_2(\eta^a,\eta^b)$ with η^a.

AMPT results on the factorization ratio $r_3(\eta^a,\eta^b)$ are shown in Fig. 15 in comparison with the CMS data for Pb+Pb collisions at 2.76 TeV [47]. We see that the AMPT results at 2.76 TeV are roughly consistent with data and that the longitudinal correlation is much suppressed for Au+Au collisions at 200 GeV, qualitatively similar to an earlier study [46]. In addition, the factorization ratio $r_3(\eta^a,\eta^b)$ at 5.02 TeV is mostly somewhat higher than that at 2.76 TeV at the same centrality. However, statistical error bars of the AMPT $r_3(\eta^a,\eta^b)$ results are often too big for us to draw more conclusions.

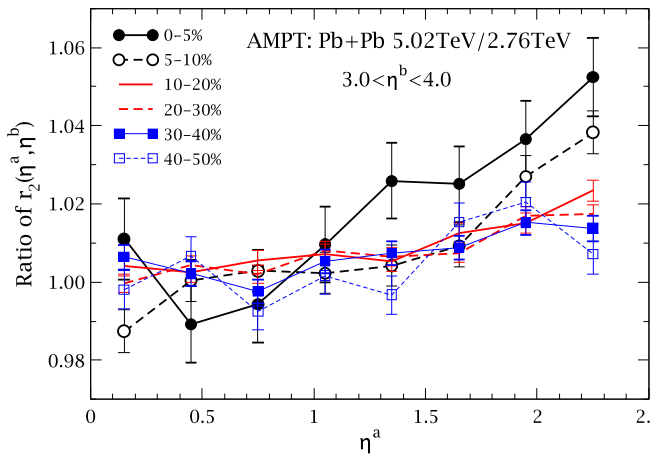

FIG. 14. Ratio of the factorization ratio $r_2(\eta^a,\eta^b)$ at 5.02 TeV to that at 2.76 TeV as a function of η^a for different centralities of Pb+Pb collisions.

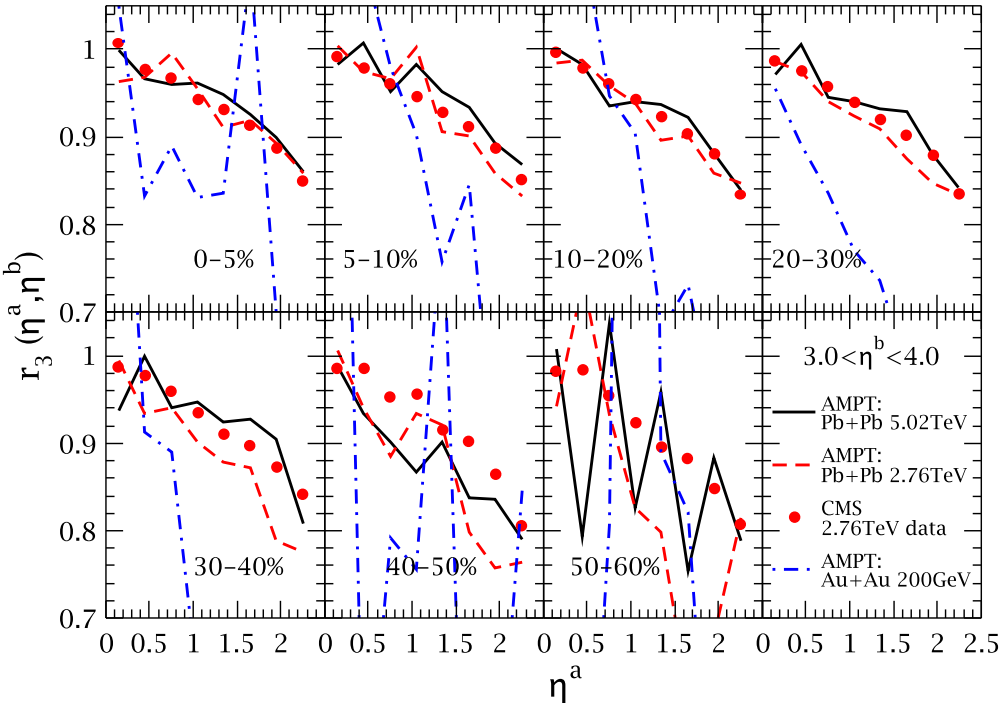

FIG. 15. Same as Fig. 13 but for factorization ratio $r_3(\eta^a,\eta^b)$.

V. DISCUSSIONS

We have seen that the string melting version of the AMPT model can describe the qualitative features of many observables, and it can often reasonably describe the experimental data quantitatively. However, we have also seen that it is sometimes inconsistent with data, for example, the centrality dependence of variables such as the mid-pseudorapidity charged particle yields as shown in Figs. 1 and 2 and $v_n(n = 2,3,4)$ as shown in Figs. 8 and 10.

Figure 16 shows that the centrality dependence of charged particle mean transverse momentum $\langle p_T \rangle$ at mid-pseudorapidity from the AMPT is also inconsistent with the CMS data at 2.76 TeV [41] and STAR data at 200 GeV [48]. Experimental data show an overall increase of $\langle p_T \rangle$ with $N_{\rm part}$, while the string melting AMPT results show an overall decrease. It was known that the string melting version of AMPT leads to a smaller $\langle p_T \rangle$ for more central collisions, while the default version of AMPT shows the opposite [49]. One reason is that in the string melting AMPT model each parton scatters more frequently on the average for more central collisions, and more collisions lead to a bigger decrease of the parton $\langle p_T \rangle$. Similar to earlier AMPT studies, in this study we use the same Lund string fragmentation a and b values for different centralities at a given energy. On the other hand, there is considerable uncertainty regarding the initial condition of heavy ion collisions, and the Lund a and b values, which controls the initial parton production including the initial parton $\langle p_T \rangle$, may depend on centrality and/or system size [5]. This will consequently affect the centrality dependence of observables calculated from the AMPT model.

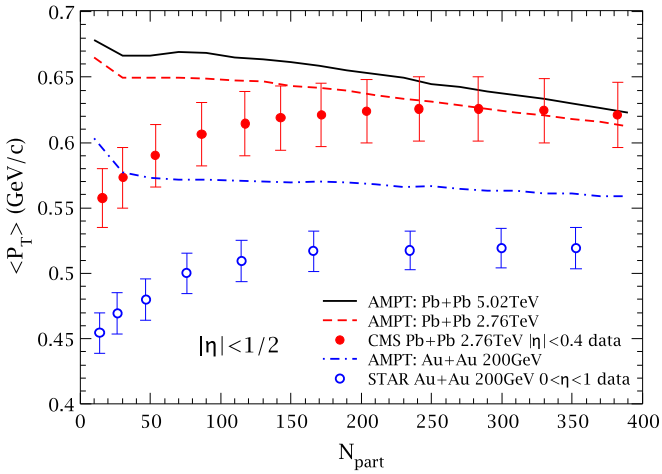

FIG. 16. AMPT results on the centrality dependence of charged particle mean transverse momentum, $\langle p_T \rangle$, at mid-pseudorapidity in comparison with the CMS data at 2.76 TeV and STAR data at 200 GeV.

Since we may expect some uncertainties to cancel out in ratios, we show in Fig. 17 the ratio of the charged particle $\langle p_T \rangle$ at mid-pseudorapidity at one energy to that at a lower energy. The ratio of the AMPT $\langle p_T \rangle$ at 2.76 TeV to that at 200 GeV (dashed curve) is seen to have a weak centrality dependence similar to the data; while the overall magnitude of the AMPT ratio is lower than the data. We also see from the AMPT results that, as the energy of Pb+Pb collisions increases from 2.76 TeV to 5.02 TeV, $\langle p_T \rangle$ at mid-pseudorapidity only increases slightly (between 1.7% and 3.0%). The overall magnitude of the $\langle p_T \rangle$ relative increase from AMPT is close to that from a recent hydrodynamic prediction [16]. However the centrality dependences are different: AMPT results show

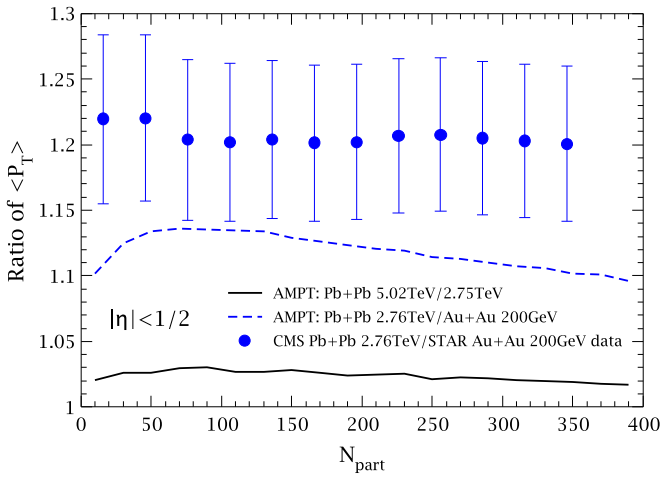

FIG. 17. Ratio of charged particle $\langle p_T \rangle$ at mid-pseudorapidity at two different energies as a function of N_{part} from AMPT in comparison with data.

a small decrease of the $\langle p_T \rangle$ ratio going from midcentral towards central collisions, while the hydrodynamic prediction [16] shows a small increase.

Proton rapidity distribution is another observable that the string melting version of the AMPT model fails to describe. It was realized earlier on [5] that the string melting version of AMPT (unlike the default version of AMPT) gives an artificial peak at midrapidity in the proton and antiproton rapidity distributions for central Au+Au collisions at 200 GeV, which points to the need to improve the simple quark coalescence model in AMPT [50]. As shown in Fig. 18(a), the string melting AMPT model also gives midrapidity peaks in both central (thick curves) and semicentral (thin curves) Pb+Pb collisions at LHC energies. In addition, the model significantly overestimates the proton dN/dy at midrapidity in comparison with the corresponding ALICE data at 2.76 TeV (filled circles). Figure 18(b) shows the proton p_T spectra at midrapidity for central collisions, where we see that the AMPT model mostly overestimates at low p_T and the overestimation factor is bigger at 2.76 TeV than that at 200 GeV. On the other hand, the elliptic flow is normalized by the particle multiplicity, therefore it is not directly affected by this overestimation. Figure 18(c) indeed shows that the proton v_2 results at midrapidity from AMPT (curves without symbols) agree reasonably well with the ALICE data at 2.76 TeV and PHENIX data at 200 GeV for the 20–30% centrality, where the AMPT v_2 results at 200 GeV has the cut $|\eta| < 0.35$ for comparison with the PHENIX data. Nevertheless, it is important to address the problem in baryon rapidity distributions in the string melting version of AMPT. Improvements of the quark coalescence model in AMPT will be needed; for example, it has been proposed that one should use the local energy density as the criterion of hadronization in order to make the effective equation of state more realistic [5,50,51].

VI. SUMMARY

Using the string melting version of a multiphase transport model with parameters established from an earlier study, we present predictions on various observables in Pb+Pb collisions at $\sqrt{s_{NN}} = 5.02$ TeV. AMPT results and experimental data for Pb+Pb collisions at 2.76 TeV and Au+Au collisions at 200 GeV are also often shown for comparisons. We first compare with the already-available centrality dependence data on charged particle $dN/d\eta$ in Pb+Pb collisions at 5.02 TeV. We then present AMPT model predictions on identified particle dN/dy, p_T spectra at midrapidity for central collisions, azimuthal anisotropies $v_n(n = 2,3,4)$ including the p_T, centrality and η dependences, and factorization ratios $r_n(\eta^a,\eta^b)(n = 2,3)$ for longitudinal correlations.

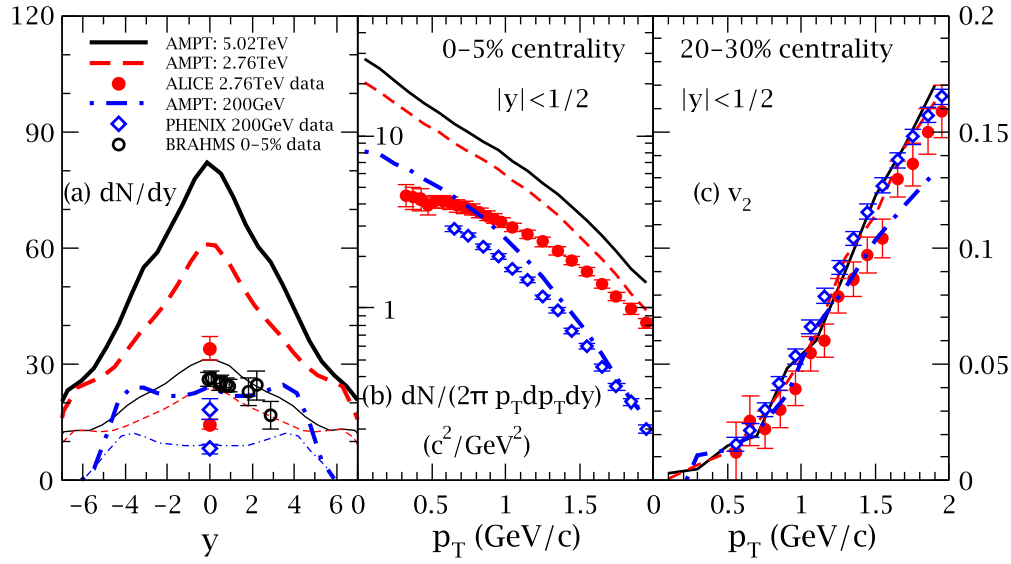

FIG. 18. AMPT results on protons in Pb+Pb collisions at 5.02 TeV, 2.76 TeV, and Au+Au collisions at 200 GeV: (a) dN/dy for 0–5% and 20–30% centralities, (b) p_T spectra at midrapidity for the 0–5% centrality, and (c) v_2 as a function of p_T at midrapidity for the 20–30% centrality. Corresponding experimental data at 2.76 TeV and 200 GeV are also shown for comparison.

ACKNOWLEDGMENTS

G.-L.M. is supported by the Major State Basic Research Development Program in China under Grant No. 2014CB845404, the National Natural Science Foundation of China under Grants No. 11522547, 11375251, and 11421505, the Youth Innovation Promotion Association of CAS under Grant No. 2013175.

[1] P. Huovinen, P. F. Kolb, U. W. Heinz, P. V. Ruuskanen, and S. A. Voloshin, Phys. Lett. B **503**, 58 (2001).
[2] B. Betz, J. Noronha, G. Torrieri, M. Gyulassy, I. Mishustin, and D. H. Rischke, Phys. Rev. C **79**, 034902 (2009).
[3] B. Schenke, S. Jeon, and C. Gale, Phys. Rev. Lett. **106**, 042301 (2011).
[4] Z. Xu and C. Greiner, Phys. Rev. C **71**, 064901 (2005).
[5] Z. W. Lin, C. M. Ko, B. A. Li, B. Zhang, and S. Pal, Phys. Rev. C **72**, 064901 (2005).
[6] W. Cassing and E. L. Bratkovskaya, Nucl. Phys. A **831**, 215 (2009).
[7] H. Petersen, J. Steinheimer, G. Burau, M. Bleicher, and H. Stocker, Phys. Rev. C **78**, 044901 (2008).
[8] K. Werner, I. Karpenko, T. Pierog, M. Bleicher, and K. Mikhailov, Phys. Rev. C **82**, 044904 (2010).
[9] H. Song, S. A. Bass, U. Heinz, T. Hirano, and C. Shen, Phys. Rev. Lett. **106**, 192301 (2011); **109**, 139904 (2012).
[10] P. Bozek, Phys. Rev. C **85**, 014911 (2012).
[11] G. L. Ma and A. Bzdak, Phys. Lett. B **739**, 209 (2014).
[12] A. Bzdak and G. L. Ma, Phys. Rev. Lett. **113**, 252301 (2014).
[13] L. He, T. Edmonds, Z. W. Lin, F. Liu, D. Molnar, and F. Wang, Phys. Lett. B **753**, 506 (2016).
[14] Z. W. Lin, L. He, T. Edmonds, F. Liu, D. Molnar, and F. Wang, arXiv:1512.06465 [nucl-th].
[15] H. Niemi, K. J. Eskola, R. Paatelainen, and K. Tuominen, Phys. Rev. C **93**, 014912 (2016).
[16] J. Noronha-Hostler, M. Luzum, and J. Y. Ollitrault, Phys. Rev. C **93**, 034912 (2016).
[17] B. Zhang, C. M. Ko, B. A. Li, and Z. W. Lin, Phys. Rev. C **61**, 067901 (2000).
[18] S. A. Bass *et al.*, Nucl. Phys. A **661**, 205 (1999).
[19] Z. W. Lin, S. Pal, C. M. Ko, B. A. Li, and B. Zhang, Phys. Rev. C **64**, 011902(R) (2001).
[20] M. Gyulassy and X. N. Wang, Comput. Phys. Commun. **83**, 307 (1994).
[21] B. Zhang, Comput. Phys. Commun. **109**, 193 (1998).
[22] T. Sjostrand, Comput. Phys. Commun. **82**, 74 (1994).
[23] B. A. Li and C. M. Ko, Phys. Rev. C **52**, 2037 (1995).
[24] Z. W. Lin and C. M. Ko, Phys. Rev. C **65**, 034904 (2002).
[25] Z. W. Lin, C. M. Ko, and S. Pal, Phys. Rev. Lett. **89**, 152301 (2002).
[26] N. Armesto *et al.*, J. Phys. G **35**, 054001 (2008).
[27] Z. W. Lin, Phys. Rev. C **90**, 014904 (2014).
[28] AMPT source files are available at http://myweb.ecu.edu/linz/ampt/.
[29] J. Adam *et al.* (ALICE Collaboration), arXiv:1512.06104 [nucl-ex].
[30] K. Aamodt *et al.* (ALICE Collaboration), Phys. Rev. Lett. **106**, 032301 (2011).
[31] S. S. Adler *et al.* (PHENIX Collaboration), Phys. Rev. C **71**, 034908 (2005).
[32] E. Abbas *et al.* (ALICE Collaboration), Phys. Lett. B **726**, 610 (2013).
[33] J. Adam *et al.* (ALICE Collaboration), Phys. Lett. B **754**, 373 (2016).
[34] B. Abelev *et al.* (ALICE Collaboration), Phys. Rev. C **88**, 044910 (2013).
[35] S. S. Adler *et al.* (PHENIX Collaboration), Phys. Rev. C **69**, 034909 (2004).
[36] I. G. Bearden *et al.* (BRAHMS Collaboration), Phys. Rev. Lett. **94**, 162301 (2005).
[37] A. M. Poskanzer and S. A. Voloshin, Phys. Rev. C **58**, 1671 (1998).
[38] S. Chatrchyan *et al.* (CMS Collaboration), Phys. Lett. B **724**, 213 (2013).
[39] G. Aad *et al.* (ATLAS Collaboration), Phys. Rev. C **86**, 014907 (2012).
[40] Y. Gu (PHENIX Collaboration), Nucl. Phys. A **904-905**, 353c (2013).
[41] S. Chatrchyan *et al.* (CMS Collaboration), Phys. Rev. C **87**, 014902 (2013).
[42] G. Aad *et al.* (ATLAS Collaboration), Eur. Phys. J. C **74**, 2982 (2014).
[43] B. B. Back *et al.* (PHOBOS Collaboration), Phys. Rev. C **72**, 051901(R) (2005).
[44] K. Xiao, F. Liu, and F. Wang, Phys. Rev. C **87**, 011901(R) (2013).
[45] L. G. Pang, G. Y. Qin, V. Roy, X. N. Wang, and G. L. Ma, Phys. Rev. C **91**, 044904 (2015).
[46] L. G. Pang, H. Petersen, G. Y. Qin, V. Roy, and X. N. Wang, Eur. Phys. J. A **52**, 97 (2016).
[47] V. Khachatryan *et al.* (CMS Collaboration), Phys. Rev. C **92**, 034911 (2015).
[48] J. Adams *et al.* (STAR Collaboration), Phys. Rev. C **70**, 054907 (2004).
[49] Md. Rihan Haque, Z. W. Lin, and B. Mohanty, Phys. Rev. C **85**, 034905 (2012).
[50] Z. W. Lin, Indian J. Phys. **85**, 837 (2011).
[51] Y. Zhang, J. Zhang, J. Liu, and L. Huo, Phys. Rev. C **92**, 014909 (2015).